Electron. Mater. Lett., Vol. 11, No. 1 (2015), pp. 13-23
DOI: 10.1007/s13391-014-4002-0

Controlling Band Gap and Refractive Index in Dopant-Free α-Fe_2O_3 Films

Pawan Kumar,[1] Nitin Rawat,[2] Da-Ren Hang,[3] Heung-No Lee,[2] and Rajesh Kumar[1,2,*]

[1]Jaypee University of Information Technology, Waknaghat, Solan 173234, Himachal Pradesh, India
[2]Gwangju Institute of Science and Technology, Gwangju 500712, Korea
[3]Department of Materials and Optoelectronic Science, National Sun Yat-sen University, Kaohsiung 804, Taiwan

(received date: 3 January 2014 / accepted date: 17 July 2014 / published date: 10 January 2015)

Dopant-free hematite (α-Fe_2O_3) films are formed at a liquid-vapor interface by means of an easy method in order to control the band gap and refractive index of the films. The α-Fe_2O_3 films after being transferred to a glass substrate are studied for their structural and optical properties. Control over the thickness of the films in the range from 75 to 400 nm and the constituent nanocrystallite size from 3 to 46 nm is achieved by controlling the synthesis parameters. By controlling the film thickness, crystallite size, and crystallinity of dopant-free α-Fe_2O_3 films, the optical band gap is increased significantly (by $\approx$ 0.64 eV) from 2.30 to 2.94 eV, along with increase in the refractive index from 1.35 to 2.8. The observed increase in the optical band gap is explained on the basis of change in lattice symmetry (via change in the c/a ratio) of α-Fe_2O_3 crystallites.

Keywords: oxide materials, optical materials, α-Fe_2O_3 thin films, band gap, and optical properties

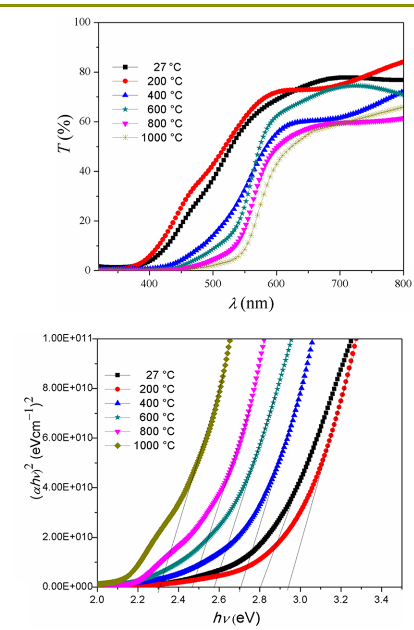

1. INTRODUCTION

The band gap and band-edge positions of semiconductors are of importance in photoelectrochemical and photocatalytical applications.[1] Iron oxide, particularly α-Fe_2O_3 has several advantages over other semiconductor materials when used to realize devices with an optical band gap of approximately 2.00 eV. It possesses excellent chemical stability over a broad range of pH values, an absorption spectrum in the wavelength region between 600 and 295 nm,[2] is abundantly available in the earth's crust, and is inexpensive and non toxic.[3] This makes α-Fe_2O_3 an attractive candidate for photoelectrochemical [PEC] water splitting,[4] optical limiting,[5] and optoelectronic applications.[6] Most of these applications require a tunable optical band gap for improved performance, e.g., an optical band gap of around 2.46 eV is necessary for water photocatalysis while using α-Fe_2O_3 without the application of any bias voltage.[7] In this light, realizing a blue shift in the band gap of hematite by an energy of about 0.3 to 0.6 eV can make hematite an ideal anode material for photocatalytic oxidation of water as well.[1,7]

In applications wherein the optical band gap of α-Fe_2O_3 requires to be greater than 2.00 eV, control of the crystallite size/thickness can enables tuning of the optical band gap. Similar to the optical band gap, the refractive index of materials is also an important factor in several optical designs/applications.[8,9] The performance of many solid state devices such as integrated optical emissive displays, optical sensors, integrated optical circuits, and light-emitting diodes can be improved by applying a high refractive index film/coating on the light emitting/sensing portion of the devices.[10-15] In fact, both the optical band gap and refractive index depend upon the crystallite size and thickness of the film.

In the backdrop of controlling crystallite size, nanostructures

*Corresponding author: rajesh.kumar@juit.ac.in

of α-Fe_2O_3 have been synthesized by numerous methods,[16-23] but the practical application of these methods has been restricted because of the high cost of synthesis equipment, limitations in achieving a large surface area, and uniform deposition of film.[24-26] Thus, a facile and cost effective method providing easy tuning of the optical band gap and refractive index of α-Fe_2O_3 film is highly desirable. The techniques reported earlier[27-29] for band gap engineering requires doping of other elements or the fabrication of nanocomposites, which are disadvantageous in terms of stability and cost effectiveness. Previously, we have reported a novel technique for the synthesis of undoped α-Fe_2O_3 films on the surface of a precursor solution at low temperature.[30] Here, the same method is adopted for the tuning of the optical properties of the band gap and refractive index of undoped α-Fe_2O_3 films. The optical properties of the films depend upon their thickness and crystallite size, and this method enables easy control over the thickness and crystallite size of the film and thus on the optical properties. In the present study, unlike the case of the quantum confinement effect on the band gap,[1,29] we observed that the variation in the optical band gap of film is dependent upon the change in lattice symmetry caused by lattice modification. When compared with reported band gap values,[31-33] a larger variation in the optical band gap of undoped α-Fe_2O_3 film is observed, which is attributed to the small crystallite size and partial amorphous nature of the film. The variation in refractive index is explained in terms of the packing density of α-Fe_2O_3 films, which is easily controlled by the synthesis parameters.

2. EXPERIMENTAL PROCEDURE

Floating films of α-Fe_2O_3 were formed on a liquid-vapor interface. A mixed solution containing 24.0 mM of $FeCl_2$ (purity 99.99%, Sigma Aldrich) and 22.0 mM of $FeCl_3 \cdot 6H_2O$ (purity 99.99%, Sigma Aldrich) was used as the precursor solution.

The floating films were transferred to glass substrates that were annealed in a horizontal tube furnace in presence of argon gas. The variation in optical properties of the films was studied with the following variations in the synthesis parameters, i.e., (i) dose (vol. %) of NH_3, (ii) concentration of polyvinyl alcohol (PVA), and (iii) the annealing temperature. The dose of NH_3 vapor was varied from 2% (40 cm^3) to 4% (80 cm^3) and then to 6% (120 cm^3) at a fixed (32 μM) concentration of PVA. The concentration of PVA was varied from 8 to 32 and then to 80 μM for a fixed dose of NH_3 at 6% (120 cm^3). The films obtained in these two sets of experiments were annealed at 500°C. In the third set, the films formed for a fixed concentration (32 μM) of PVA and a fixed dose of NH_3 (6% (120 cm^3)) were annealed at 200°C, 400°C, 600°C, 800°C, and 1000°C. These films were characterized for a study of their structural and optical properties. The structural properties were examined using an x-ray diffractometer (XRD, PANalytical's X'Pert-PRO) and

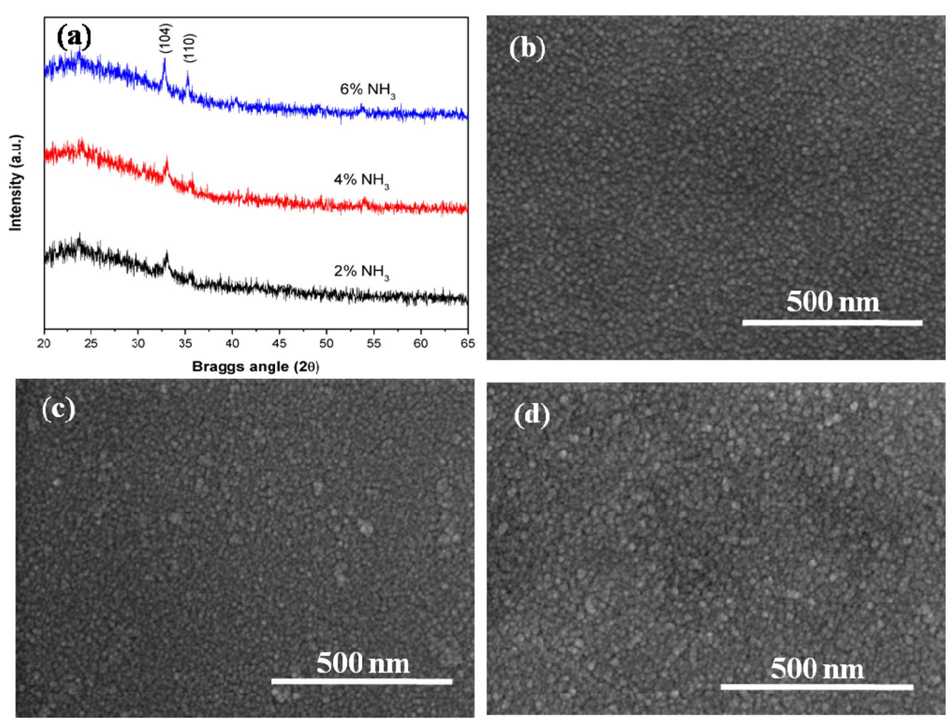

Fig. 1. (a) XRD patterns of α-Fe_2O_3 films obtained with 2%, 4%, and 6% NH_3 doses. The films were annealed at 500°C. (b), (c), and (d) SEM images of films formed with 2, 4, and 6% NH_3 doses, respectively.

a transmission electron microscope (TEM, JEOL, JEM 2100), the morphological properties were studied via a scanning electron microscope (SEM, Hitachi, S-4700), and the film thickness was examined using a Stylus profilometer. The optical properties were studied using a UV-Vis-NIR double-beam spectrophotometer (Perkin Elmer Lambda-750) in the 250 - 900 nm wavelength range.

3. RESULTS AND DISCUSSION

3.1 Variation in optical properties with NH_3 dosage

For all three sets of experiments, we analyzed the morphological and structural changes in the films. We first discuss the films formed under the condition when the NH_3 dose was varied. Figure 1(a) shows the XRD images of films formed for 2%, 4%, and 6% doses of NH_3. The films were investigated using XRD with a Cu Kα (1.54 Å) source and scanning angles ranging from 20° to 65° with a step size of 0.01 at room temperature. The XRD plot shows diffraction peaks corresponding to α-Fe_2O_3 (according to JCPDS-ICCD PDF card No. 33-0664). Crystalline peaks around 32.4° and 35.4° correspond to the (104) and (110) planes of α-Fe_2O_3, thereby indicating its hexagonal (corundum-type) structure. The XRD shows that the intensity of the crystalline peaks increases with NH_3 dose which may be due to increasing thickness of the α-Fe_2O_3 film as obtained by profilometer data (Table 1). The increase in thickness of the α-Fe_2O_3 film with increasing doses of NH_3 is due to the presence of a large number of NH_3 molecule within the reaction chamber that react with a large number of precursor ions (Fe^{3+}/Fe^{2+}) on the solution surface, thereby resulting increased film thickness. The average crystallite size (D) in α-Fe_2O_3 films is estimated using Scherrer's formula,[34] $D = 0.9\lambda/\beta\cos\theta$, where β denotes the full width at half maximum and λ the wavelength of x-rays. The average crystallite sizes with the corresponding lattice parameters are listed in Table 1. As the film thickness increases, the size of crystallites in the film also increases as can be observed from Table 1, and this behavior is in accordance with other reports.[35] Figures 1(b) to 1(d) show the SEM images of α-Fe_2O_3 films prepared with 2, 4, and 6% NH_3 doses respectively. The increasing thickness of the film with increase in the NH_3 dosage gives rise to clustering of α-Fe_2O_3 particles, which leads to an increase in the film's roughness as indicated in SEM images (Figs. 1(b) to 1(d)).

As regards the optical properties, a UV-Vis-NIR spectrophotometer was used to observe the variation in the optical band gap and refractive index of α-Fe_2O_3 films. The obtained transmission (T) spectra with respect to variation in the NH_3 dosage are shown in Fig. 2(a). There is a decrease in the transmission of α-Fe_2O_3 films with increase in NH_3 dosage. This decrease in transmission is attributed to increase in the size of the clustered nanocrystals and the thickness of the film. Due to clustering of nanocrystallites, the increased roughness of the films enhances the scattering of light and a consequent reduced transmittance.[36] From the transmission spectra, the optical absorption coefficient α was calculated using[37] $\alpha = (1/t)\ln(1/T)$, where t denotes the thickness of the film. Further, the optical band gap (E_g) was calculated

Table 1. Values of NH_3 dosage, PVA concentration, average thickness (t), crystallite size (D), lattice parameters ($a = b$, c), optical band gap energy (E_g), refractive index (n), and relative density (ρ_f/ρ_b) for α-Fe_2O_3 films.

Dose of NH_3	PVA Concentration	Thickness (t) (nm)	D (nm) from XRD	$a = b$ (Å)	c (Å)	c/a (Å)	E_g (eV)	n (at 589 nm)	ρ_f/ρ_b
2%	32 μM	75	14.24 ± 0.81	5.06	13.92	2.75098	2.72	1.35	0.265
4%	32 μM	155	15.05 ± 1.01	5.05	13.88	2.74851	2.56	1.54	0.379
6%	32 μM	350	19.70 ± 2.30	5.05	13.86	2.74455	2.35	2.32	0.692

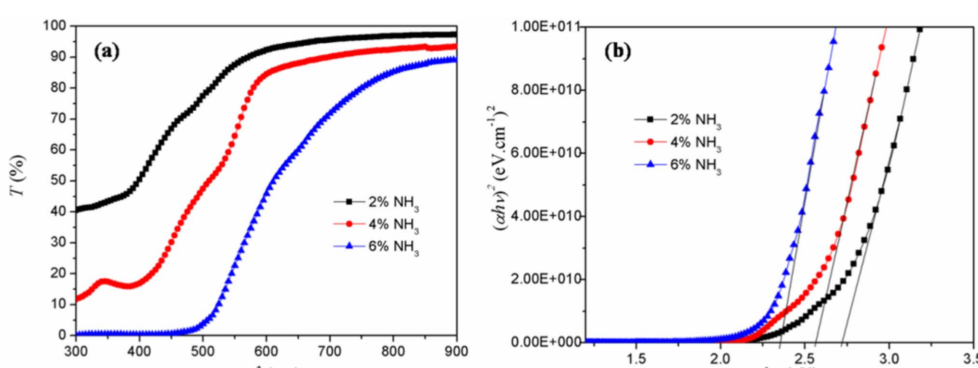

Fig. 2. (a) Transmission (T) spectra of α-Fe_2O_3 film obtained with 2, 4, and 6% doses of NH_3 and (b) plots of $(\alpha h\nu)^2$ vs $h\nu$ for these α-Fe_2O_3 films.

using the Tauc relation[38] $\alpha h\nu = C_1(h\nu - E_g)^n$, where C_1 denotes a constant, h the Planck's constant, and the prefix n = 0.5 for a direct optical band gap transition.

The calculated optical direct band gap values were 2.72, 2.56, and 2.35 eV, respectively, for 2%, 4%, and 6% doses of NH_3, and these results indicate that the optical band gap decreases with increase in film thickness. We attribute that the variation in the optical band gap to (i) stress-induced distortion of the optical band gap by film/substrate interactions, (ii) density of dislocation, (iii) quantum size effect, (iv) change in grain boundary barrier height due to change in crystallite size in the polycrystalline film,[39] and (v) change in lattice symmetry.[31] In our case, as all the films were prepared under similar synthesis conditions on similar substrates, factors (i) and (ii) may be ignored. The quantum confinement effect is mostly observed in crystallites with sizes less than 6 nm (for α-Fe_2O_3 crystallites).[1,29,40] The barrier height depends upon the crystallite size D according to the expression[41] $E_b = E_{bo} + C(X - fD)^2$, where the original barrier height E_{bo}, constant C, barrier width X, and f are specific to the materials. In our case, the variation in the crystallite size is negligible (~14 to 19 nm), and therefore, we speculate that the change in barrier height is also negligible in its contribution to the change in the band gap.

Lattice modification has been reported to affect the electronic energy levels of α-Fe_2O_3 nanocrystals.[31] A decrease in the size of α-Fe_2O_3 nanocrystallites is reported to be equivalent to the application of negative pressure, which is expected to lower the lattice symmetry owing to the anisotropic nature of the α-Fe_2O_3 lattice with a consequent increase in the axial ratios c/a, as can be observed from the values listed in Table 1.[31] We note that size-induced lattice modification (c/a) yields distinct electronic (or magnetic) properties of α-Fe_2O_3 nanocrystals.[31] An increase in the c/a ratio results in an increase in ionicity and Fe-O bond separation during the anisotropic expansion of smaller size crystallite. The most intense absorption peak of α-Fe_2O_3[31,42] is given by the expression $E = -10Dq + 10B + 6C - 26B^2/10Dq$, where $10Dq$ denotes the crystal field splitting, and B and C the Racah parameters that describe the neighboring covalency effect in a transition metal system.[31] The second-order term ($-26B^2/10Dq$) is extremely small compared to the sum of the terms $10B$ and $6C$ according to the estimated ligand field theory parameters.[31] Since the Racah parameters B and C increase with decrease in nanocrystallite size under low pressure,[42] the observed blue shift (band gap change) in the absorption peak of the α-Fe_2O_3 film with reduced crystallite size is likely the consequence of increase in the magnitude of the Racah parameters.

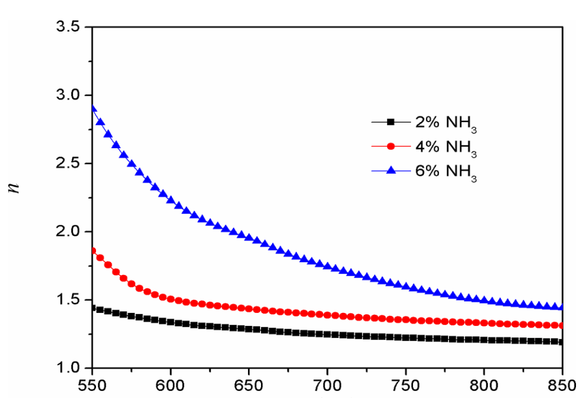

Fig. 3. Refractive index (n) vs wavelength (λ) plots of α-Fe_2O_3 films obtained with 2%, 4%, and 6% doses of NH_3.

To calculate the refractive index of α-Fe_2O_3 films, the reflectance was determined by using the expression[42] $R = 1 - [T \exp(A)]^{1/2}$, where A denotes the absorption of the film. Finally, the refractive index (n) of the films was calculated using the approximation[43,44] $n = [(1 + R) / (1 - R)] + [((4R)/(1 + R)^2) - (k)^2]^{1/2}$, where k denotes the extinction coefficient related to the absorption coefficient (α) as $k = \alpha\lambda/4\pi$. We observed that at a particular wavelength, the refractive index of the film increases with the NH_3 doses, as shown in Fig. 3. The increase in refractive index with increasing film thickness can be attributed to an increase in the packing density of the film that is concurrent with increase in the film thickness. As the film thickness increases, its porosity decreases,[45] thereby resulting in increased refractive index of the film. The increased size of the crystallites in the film increases its density due to the reduced crystallite boundaries[46-48] and consequently, this contributes to increase in the refractive index. The film density was calculated by using the Lorentz-Lorenz relation,[49] $\rho_f/\rho_b = [(n_f^2 - 1)(n_b^2 + 2)]/[(n_f^2 + 2)(n_b^2 - 1)]$, where ρ_f denotes the density of the α-Fe_2O_3 film, ρ_b the density of bulk α-Fe_2O_3, n_f the refractive index of the film, and n_b the refractive index of bulk material (n_b = 3.003 at λ = 633 nm).[36] For n_f values of 1.31, 1.47, and 2.01 corresponding to films formed with 2%, 4%, and 6% doses of NH_3, respectively, the calculated relative densities (ρ_f/ρ_b) are listed in Table 1. The results indicate that with increase in the NH_3 dose, the thickness as well as the size of nanocrystallites in the α-Fe_2O_3 film increases, which results in an increase in the packing density and refractive index of the film.

3.2 Variation in optical properties with PVA concentration

The XRD patterns of the films obtained with various PVA concentration values are shown in Fig. 4(a). Here, the XRD peak intensity decreases with increasing PVA concentration. This decrease in the peak intensity is due to decrease in the crystalline nature of film via the PVA capping effect.[50] Based on calculations from the XRD data (Table 2), we obtain the crystallite sizes for PVA concentrations of 8, 32, and 80 μM as 26.80, 14.6, and 12.26 nm, respectively. The SEM images in Figs. 4(b) to 4(d) also exhibit a change in the

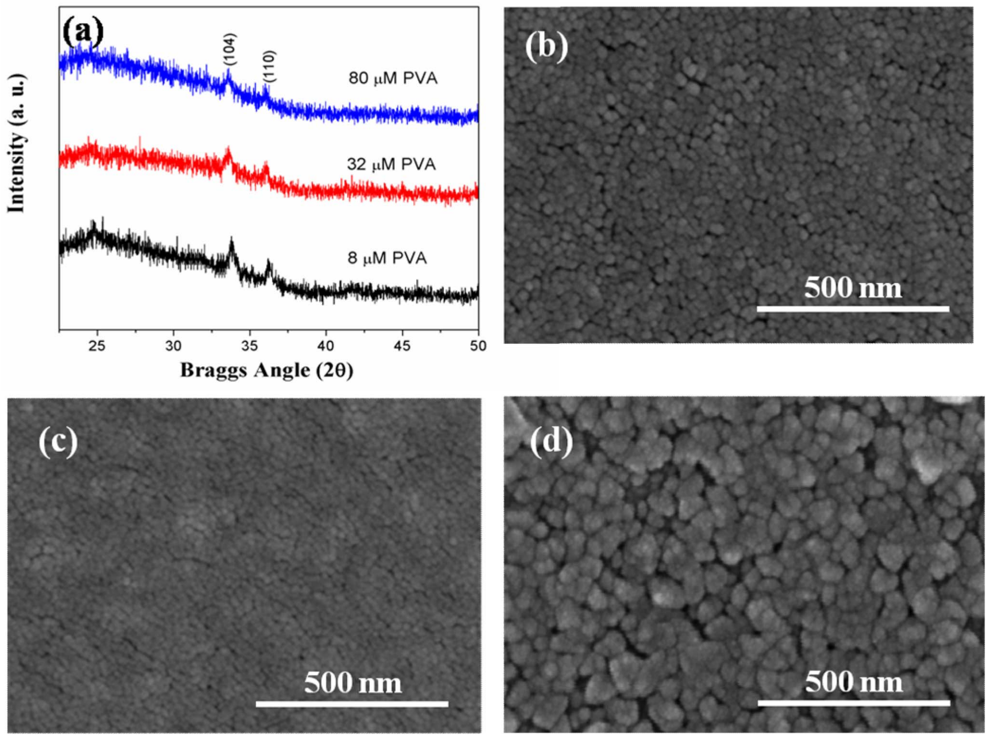

Fig. 4. (a) XRD patterns and (b), (c), and (d) SEM images of α-Fe_2O_3 films formed at 8, 32, and 80 μM PVA concentrations, respectively.

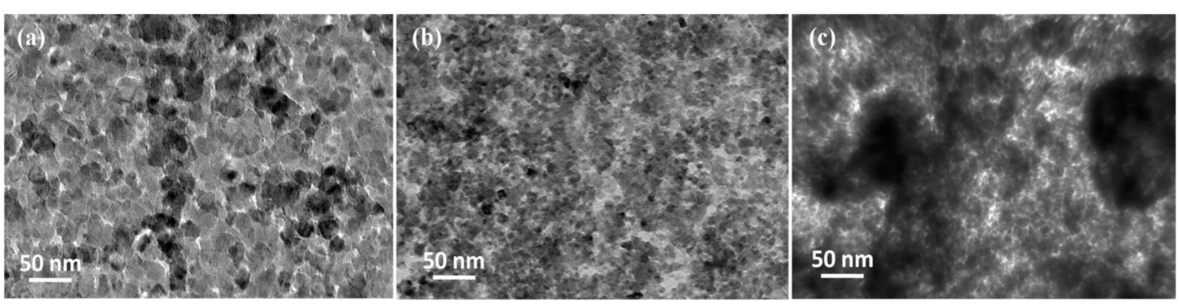

Fig. 5. TEM images of α-Fe_2O_3 films formed at 6% dose of NH_3 with (a) 8, (b) 32, and (c) 80 μM PVA concentrations.

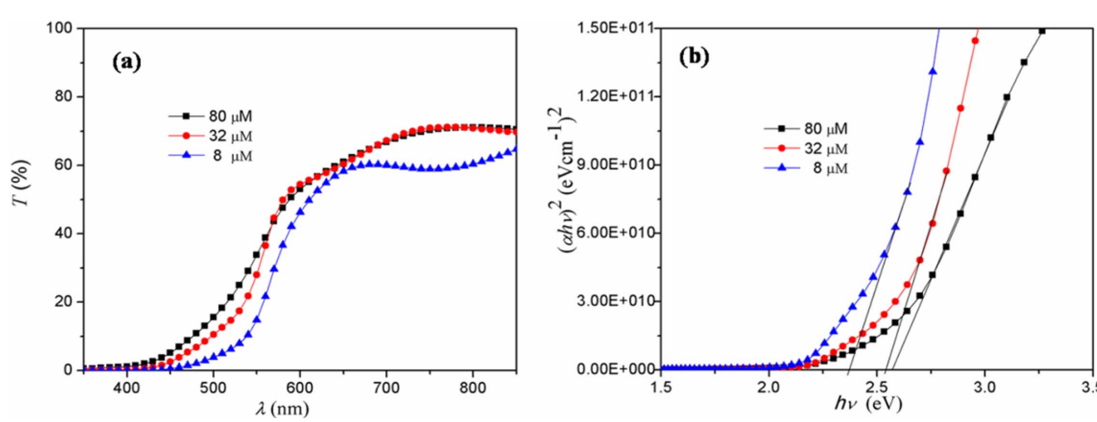

Fig. 6. (a) Transmission (T) spectra of α-Fe_2O_3 films formed at 8, 32, and 80 μM PVA concentrations, and (b) $(\alpha h\nu)^2$ vs $h\nu$ plot of the films.

Table 2. Values of PVA concentration, NH_3 dosage, average thickness (t), crystallite size (D), lattice parameters (a = b, c), optical band gap energy (E_g), refractive index (n), and relative density (ρ_f/ρ_b) for α-Fe_2O_3 films.

PVA concentration	Dose of NH_3	Thickness (t) (nm)	D (nm) from XRD	a=b (Å)	c (Å)	c/a (Å)	E_g (eV)	n (at 589 nm)	ρ_f/ρ_b
8 μM	6%	398	26.80 ± 2.82	4.98	13.55	2.72088	2.37	2.30	0.6857
32 μM	6%	401	14.60 ± 1.10	4.99	13.66	2.73747	2.54	2.13	0.6637
80 μM	6%	396	12.26 ± 0.87	5.02	13.78	2.74502	2.57	2.09	0.5323

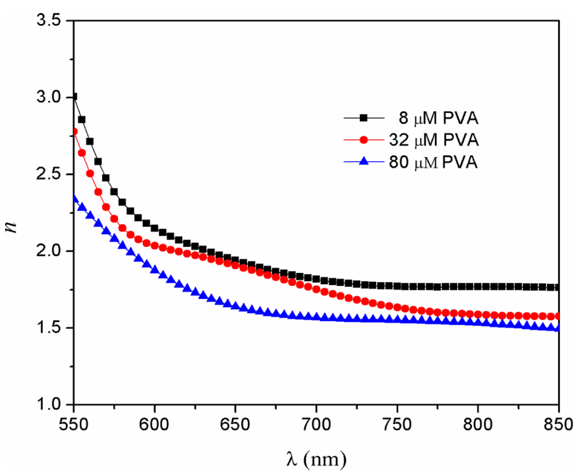

Fig. 7. Refractive index (n) vs wavelength (λ) plots of α-Fe_2O_3 films formed at 8, 32, and 80 μM PVA concentrations.

morphology of the films with increasing concentration of PVA. Figure 4(d) shows an aggregation of small nanoparticles, which is confirmed by the XRD data and the TEM image in Fig. 5(c). From the TEM image, it is observed that the larger nanoparticles are aggregations of smaller nanoparticles, as reported in a previous study.[30] Figures 5(a) to 5(c) show TEM images corresponding PVA concentrations of 8, 32, and 80 μM, respectively. It is clear from the TEM images that small nanocrystallites aggregate with increasing PVA concentration. We conclude that for a particular dose of NH_3, increasing the PVA concentration results in a decrease in the nanocrystallite size (although they are aggregated).

As regards optical properties, the α-Fe_2O_3 films show increased transmission with increasing PVA concentration from 8 to 32 μM, as shown in Fig. 6(a). The increased transmission with increasing PVA concentration is due to reduction in the crystallinity of the films. The crystallinity of the film increases as the crystallites size increases because the increased crystallite size results in the reduction of nanocrystallites boundaries due to coalition of small crystallites.[48] However in our case, the situation is opposite; as the concentration of PVA is increased, the crystallite size decreases, and hence, decreased crystallinity leads to increased transmission. On the other hand, we observed that for PVA concentrations ranging from 32 to 80 μM, the transmission remains unchanged (Fig. 6(a)). This may be due to increase in transmission being counteracted by increase in light scattering. An increase in light scattering is expected due to increasing roughness caused by the aggregation of small nanocrystallites with increase in PVA concentration. The blue shift in the transmission spectra (Fig. 6(a)) with increasing concentration of PVA indicates an increasing optical band gap in the α-Fe_2O_3 films. Figure 6(b) shows the increase in the optical band gap from 2.37 to 2.54 and then to 2.57 eV corresponding to PVA concentrations of 8, 32, and 80 μM. In this case as well the band gap variation can be explained on the basis of change in the lattice symmetry in a manner similar to the case of NH_3. The parameters related to change in PVA concentration are listed in Table 2.

Next, we examine the change in the refractive index with increasing PVA concentration. The refractive index decreases with increasing PVA concentration, as shown in Fig. 7, which is again due to variation in the density of the α-Fe_2O_3 films. In this case, the trend is opposite to that observed in case when ammonia dosage is increased, i.e., the density of the film decreases (Table 2) with increasing PVA concentration unlike the case of increasing NH_3 dosage.

The density of the films decreases due to the increasing porosity of α-Fe_2O_3 nanocrystals in the film with increasing concentration of PVA.[51] The PVA molecules that are flexible penetrate the voids between clusters of α-Fe_2O_3 nano crystallites, and when the films are annealed, the PVA molecule evaporate leaving large voids within the α-Fe_2O_3 nanocrystallites, thereby making them mesoporous. This increase in the porosity (decrease in packing density of α-Fe_2O_3 films) with increasing PVA concentration results in a decrease in the refractive index of the films. From the application point of view, these mesoporous α-Fe_2O_3 nanostructures are highly desirable in many applications such as lithium-ion batteries[52] gas sensors,[53] and photochemical[54] and photoelectrochemical applications.[54]

In the above mentioned set of experiments, we observed that the synthesis parameters i.e., dosage of NH_3 and PVA concentration, significantly affect the optical properties of α-Fe_2O_3 films. We also observed that annealing temperature is also an important factor for the tuning of the optical properties of the films,[55] and therefore we examined the combined effect of annealing temperature along with variation in these synthesis parameters in our third set of

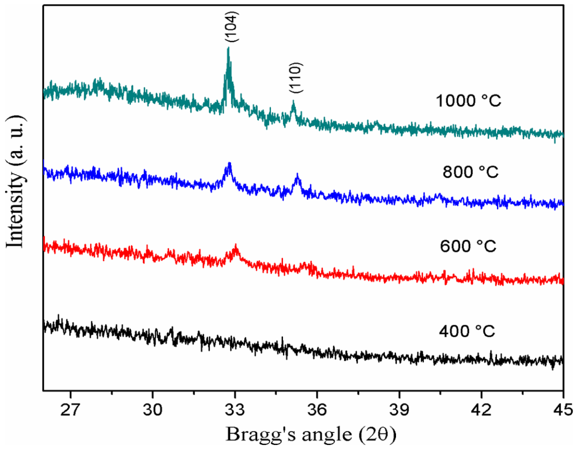

Fig. 8. XRD patterns of α-Fe_2O_3 films annealed at 400°C, 600°C, 800°C, and 1000°C.

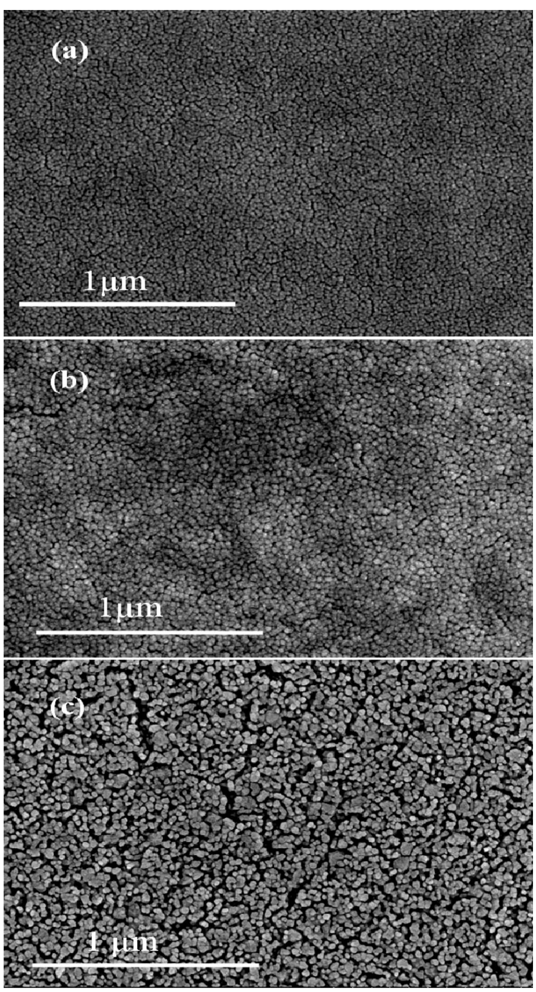

Fig. 9. SEM images of α-Fe_2O_3 films annealed at (a) 600°C, (b) 800°C, and (c) 1000°C.

experiments. As regards this set of experiments, we fixed the NH_3 and PVA concentrations and varied only the annealing

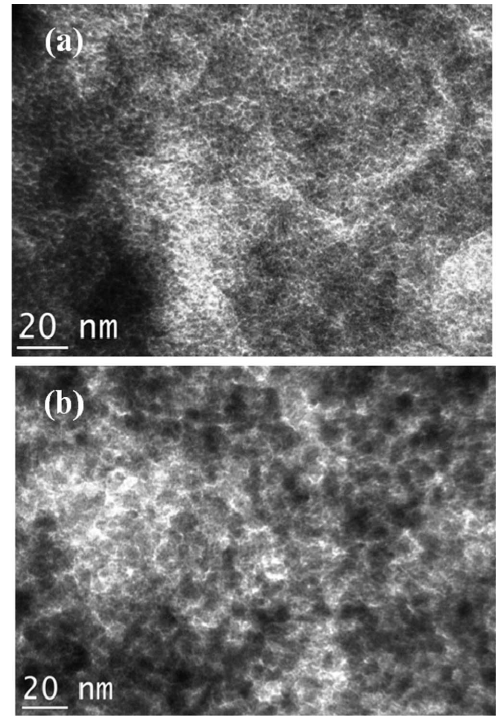

Fig. 10. TEM images of α-Fe_2O_3 films annealed at (a) 200°C, and (b) 400°C.

temperature, as discussed in following section.

3.3 Variation in optical properties with annealing temperature

To study the effect of annealing temperature on the films, we selected an α-Fe_2O_3 film formed at 6% dosage of NH_3 and a PVA concentration of 32 μM. The α-Fe_2O_3 films were annealed in an argon environment at 200°C, 400°C, 600°C, 800°C, and 1000°C. The films were characterized for structural and optical properties as in the previous cases. We observed that unheated films and those annealed at 200°C, and 400°C exhibited no XRD peak. This is probably due to the amorphous nature of the films below 400°C. Figure 8 shows the XRD patterns of films annealed at and above 400°C. Here, only the films annealed above 400°C exhibit crystalline XRD peaks. Further, our calculation from XRD data indicate that for the film annealed at 600°C, the average crystallite size is 24 nm, and this size increased to 31 nm and then to 46 nm for annealing temperatures of 800°C and 1000°C. The variation in the nanocrystallites sizes of the samples annealed at 600°C, 800°C, and 1000°C can also be observed in the SEM images shown in Fig. 9.

Since no XRD peaks were observed for films annealed at 200°C and 400°C, in order to estimate the crystallite sizes in these films, the corresponding TEM images (Fig. 10) were processed by using Image J software package. These samples exhibited nanocrystallite sizes of approximately

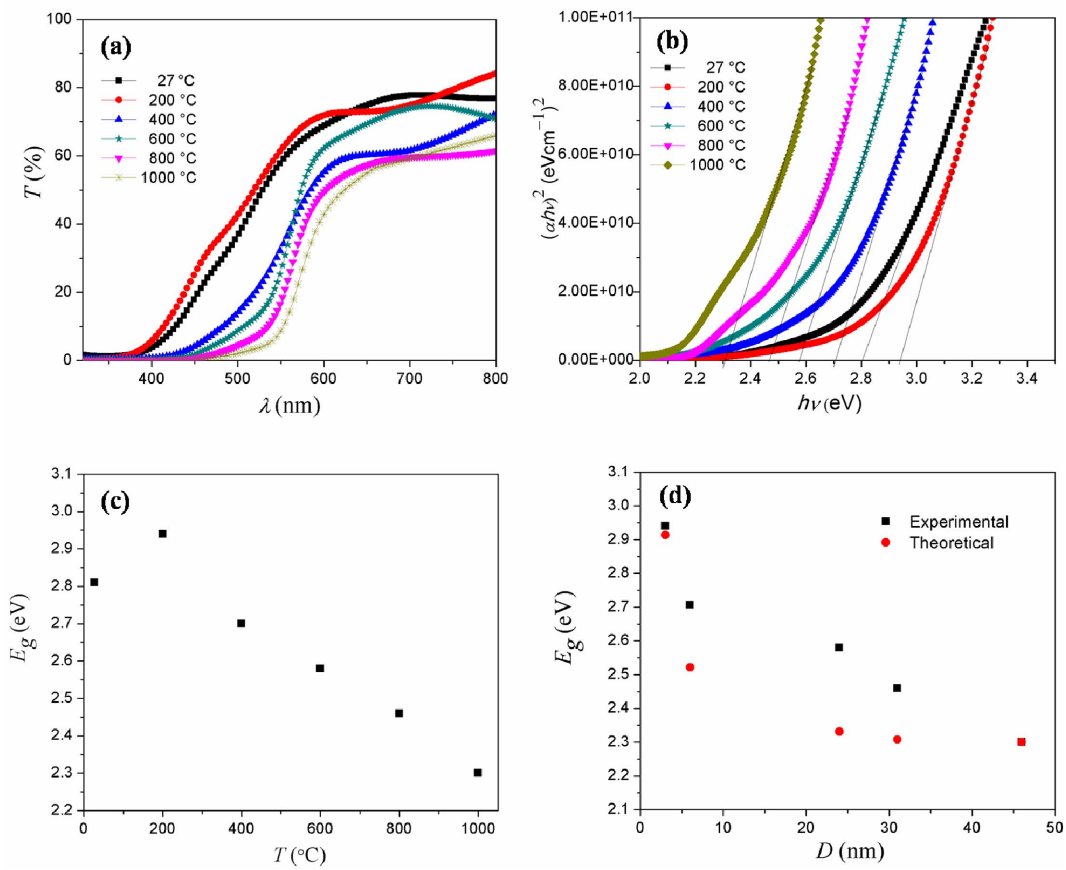

Fig. 11. (a) Transmission spectra of α-Fe_2O_3 films annealed at 200°C, 400°C, 600°C, 800°C, and 1000°C, (b) plots of $(\alpha h\nu)^2$ vs $h\nu$ of α-Fe_2O_3 films, (c) variation in optical band gap (E_g) with annealing temperature, and (d) optical band gap vs crystallite size for experimental and theoretical values.

3 nm (200°C) and 6 nm (400°C). The increase in crystallite size with increasing annealing temperature indicates that the crystalline particle size in the film can be varied by varying either the dosage of NH_3, concentration of PVA, or annealing temperature.

Figure 11(a) shows the transmission spectra of these films. With increase in annealing temperature, the transmission decreases and a red shift is observed. The decrease in the transmission of α-Fe_2O_3 films with increased annealing temperature is due to the increasing crystallite size with increasing temperature and increasing roughness caused by the formation of large nanocrystallites that increase scattering.[56,57] The density of the crystallite boundaries in the film decreases due to the increasing crystallite size (crystallinity) as well as reflection, which enhances the absorption, thereby leading to reduced transmission.[48,58-60] However, the film in the SEM image (in Fig. 9(c)), appears to be porous when compared with the films shown in Figs. 9(a) and 9(b); nevertheless, the film simultaneously (Fig. 11(a)) exhibits decreased transmission, which indicates that the porosity may exist only at the surface of the film and the overall porosity of the film does not affect the transmittance as much the crystallinity of the film does.

The optical band gaps for films annealed at 200°C, 400°C, 600°C, 800°C, and 1000°C temperatures are obtained as 2.94, 2.70, 2.58, 2.46, and 2.30 eV, respectively. The maximum band gap of 2.94 eV is obtained for the sample annealed at 200°C, which band gap value decreases with increasing annealing temperature, as shown in Figs. 11(b) and 11(c).

As regards our experiments in varying the annealing temperature, we can classify α-Fe_2O_3 films into two categories: films that exhibit the quantum size effect as they have crystallite sizes less than 5 or 6 nm and those that do not exhibit the quantum size effect as they have relatively larger crystallite sizes (their blue shift is due to only the change in lattice symmetry). The crystallite-size dependence of the optical band gap due to quantum confinement is expressed by the equation[31] $E_g = E_g^o + n^2\hbar^2\pi^2/2\mu R^2 - 1.8\, e^2/\varepsilon R$, where E_g^o can be assumed as the lowest value of the band gap[29] obtained in our experiment, R denotes the size of the crystallite, e the electronic charge, ε the dielectric constant, and μ the effective electron and hole masses. It is known that smaller crystallites in the film exhibit a larger optical band

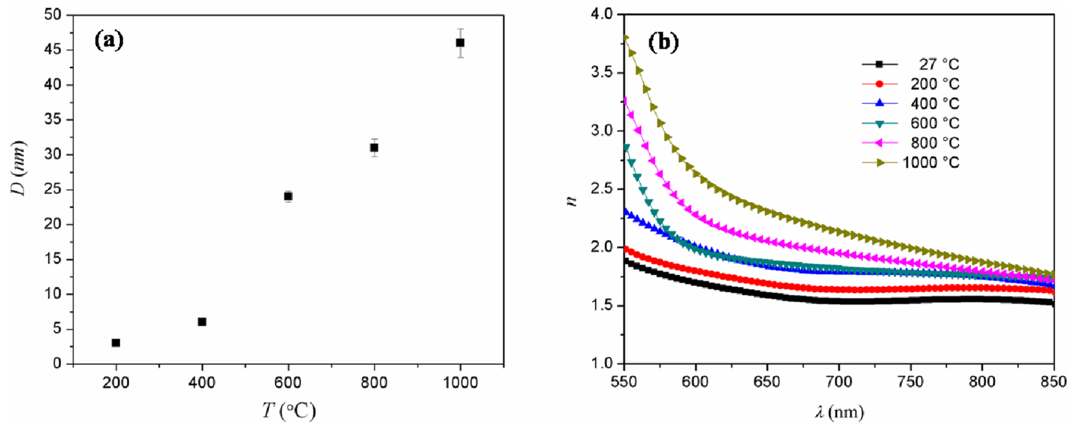

Fig. 12. (a) Plot of crystallite size (D) vs annealing temperature and (b) variation in refractive index (n) as a function of wavelength (λ) of the unheated and annealed α-Fe_2O_3 films at different temperatures.

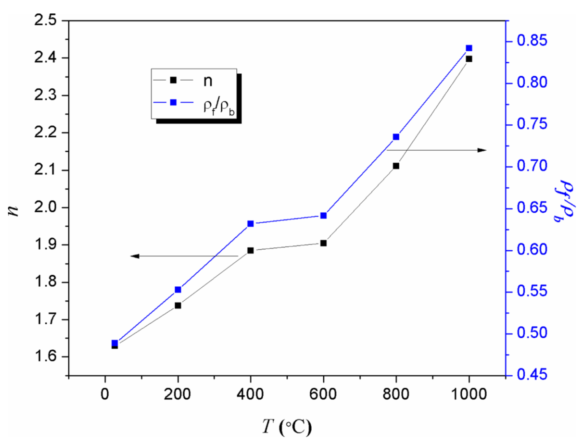

Fig. 13. Variation in refractive index (n) and relative density (ρ_f/ρ_b) with annealing temperature.

gap due to the quantum size effect and therefore, we observed a blue shift in the 3 nm crystallite film (Fig. 11(d)).[29] In Fig. 11(d), we observe that the experimental value of the band gap for the 3 nm crystallite size coincides with the theoretical value, thereby indicating that this film exhibits the quantum size effect. On increasing the crystalline size above 3 nm by increasing the annealing temperature, a deviation between experimental and theoretical values is observed, as shown in Fig. 11(d). The reason for this observed deviation is speculated to be due to the partial amorphous nature[61] of α-Fe_2O_3 films along with the change in the lattice symmetry of α-Fe_2O_3 crystallites. The resultant absorption of photons is due to both the amorphous and nanocrystalline phases of α-Fe_2O_3 particles, and hence, the absorption edges in the experimental results exhibit a higher blue shift than the theoretical values.

As regards the second category of α-Fe_2O_3 films, other studies have also reported variations in the band gap with change in the annealing temperature due to change in lattice symmetry.[32] In fact, the phase sharing of the octahedral dimer and the electrostatic repulsion of the Fe^{3+} cation are responsible for the trigonal distortion of the octahedran, thereby giving rise to C_{3v}-type symmetry.[33] With appropriate thermal treatment, the crystallite size of the α-Fe_2O_3 films increases and the structure relaxes to maximize the distance between two iron cations in Fe_2O_9 dimers.[32] As the annealing temperature is increased, the average crystallite size increases, and hence, the optical band gap decreases (Fig. 11(c)). The variation in the crystallite size in α-Fe_2O_3 films with annealing temperatures is shown in Fig. 12(a). Here, the calculated c/a ratios corresponding to α-Fe_2O_3 films annealed at 600°C, 800°C, and 1000°C are 2.749, 2.739, and 2.732, respectively. As the c/a ratio decreases with increasing annealing temperature, the films exhibit structural relaxation, which leads to decrease in the optical band gap.

Finally, the variation in the refractive index (1.7 to 2.8 at 589 nm) of these films formed with increasing annealing temperature is shown in Fig. 12(b). As expected, the α-Fe_2O_3 films show an increase in the refractive index with annealing temperature.[62,63] The variation in the refractive index with annealing temperature can be correlated with the packing density of the films as in the previous cases. From Fig. 13, we observe that the films annealed at lower temperatures have lower packing densities than those annealed at higher temperatures.

The lower packing density at lower annealing temperatures is due to the incorporation of oxygen during film growth,[36] which creates voids on annealing. As the annealing temperature increases, the increase in thermal energy facilitates the coalition of small crystallites, which increases the packing density of α-Fe_2O_3 films due to reduction in the number of voids.[64,65] In conclusion, we note that our method facilitates greater control over the tuning of the optical properties of α-Fe_2O_3 films by varying either one, two or all three process parameters, i.e., NH_3 dosage, PVA concentration, and annealing temperature.

4. CONCLUSIONS

We tailored the structural and optical properties of α-Fe_2O_3 films formed on the surface of a precursor solution. In our method the parameter of NH_3 dosage can be used to easily control the thickness of a floating α-Fe_2O_3 film on the surface of a precursor solution, and the PVA concentration in the precursor solution can be used to control the size of nanocrystallites composing the film. Lattice modification due to the change in lattice symmetry with the α-Fe_2O_3 crystallite size is speculated as the reason for the observed shift in the band gap. Further, the refractive index also changes due to change in the packing density of α-Fe_2O_3 films. The post-synthesis annealing temperature can be varied to control the size of the resultant crystalline particles, which can be utilized to further tune the optical band gap and refractive index of α-Fe_2O_3 films. Our method can significantly affect the optical band gap without the use of any dopant, and therefore, the α-Fe_2O_3 films obtained using our method are suitable for hydrogen generation from water via photocatalysis without the application of a bias voltage.

ACKNOWLEDGEMENTS

This study was supported by a Research Grant for Nanotechnology Lab, Jaypee University of Information Technology, Waknaghat, Solan (India) and the National Research Foundation of Korea (NRF) Grant funded by the Korean government (MEST) (No. 2012-0005656).

REFERENCES

1. L. Vayssieres, C. Sathe, S. M. Butorin, D. K. Shuh, J. Nordgren, and J. Guo, *Adv. Mater.* **17**, 2320 (2005).
2. M. Chirita and I. Grozescu, *Chem. Bull. "POLTECHNICA" Univ. (Timisoara)* **54**, 1 (2009).
3. R. Al-Gaashani, S. Radiman, N. Tabet, and A. R. Daud, *J. Alloy. Compd.* **550**, 395 (2013).
4. S. Shen, C. X. Kronawitter, J. Jiang, S. S. Mao, and L. Guo, *Nano Res.* **5**, 327 (2012).
5. H. A. Garcia, R. P. de Melo Jr., A. Azevedo, and C. B. de Arau'jo, *Appl. Phys. B* **111**, 313 (2013).
6. T. Hayakawa and M. Nogami, *Sci. Technol. Adv. Matter.* **6**, 66 (2005).
7. Y. Matsumoto, *J. Solid State Chem.* **126**, 227 (1996).
8. C. Liu and B. Yang, *J. Mater. Chem.* **19**, 2884 (2009).
9. S. D. Hart, G. R. Maskaly, B. Temelkuan, P. H. Prideaux, J. D. Joannopoulos, and Y. Fink, *Science* **296**, 510 (2002).
10. B. G. Prevo, Y. Hwang, and O. D. Velev, *Chem. Mater.* **17**, 3642 (2005).
11. N. Nishimuura, Y. Shibasaki, M. Ozawa, and Y. Oishi, *J. Photopolym. Sci. Technol.* **25**, 355 (2012).
12. A. Kasikov, J. Aarik, H. Mändar, M. Moppel, M. Pärs, and T. Uustare, *J. Phys. D: Appl. Phys.* **39**, 54 (2006).
13. S. Wu, G. Zhou, and M. Gu, *Opt. Mater.* **29**, 1793 (2007).
14. X. Wei, H. Shi, X. Dong, Y. Lu, and C. Du, *Appl. Phys. Lett.* **97**, 011904 (2010).
15. J. G. Liu and M. Ueda, *J. Mater. Chem.* **19**, 8907 (2009).
16. L. Zhenmin, L. Xiaoyong, W. Hong, M. Dan, X. Chaojian, and W. Dan, *Nanotechnology* **20**, 245603 (2009).
17. A. Duret and M. Gratzel, *J. Phys. Chem. B* **109**, 17184 (2005).
18. N. T. Hahn, H. C. Ye, D. W. Flaherty, A. J. Bard, and C. B. Mullins, *ACS Nano* **4**, 1977 (2010).
19. T. J. LaTempa, X. J. Feng, M. Paulose, and C. A. Grimes, *J. Phys. Chem. C* **113**, 16293 (2009).
20. A. Kay, I. Cesar, and M. Gratzel, *J. Am. Chem. Soc.* **128**, 15174 (2006).
21. K. Woo, H. J. Lee, J. P. Ahn, and Y. S. Park, *Adv. Mater.* **15**, 176 (2003).
22. S. K. Mohapatra, S. E. John, S. Banerjee, and M. Mishra, *Chem. Mater.* **21**, 3048 (2009).
23. P. M. Rao and X. L. Zheng, *Nano Lett.* **9**, 3001 (2009).
24. G. Wang, Y. Ling, D. A. Wheeler, K. E. N. George, K. Horsley, C. Heske, J. Z. Zhang, and Y. Li, *Nano Lett.* **11**, 3503 (2011).
25. D. A. Wheeler, G. Wang, Y. Ling, Y. Li, and J. Z. Zhang, *Energy Environ. Sci.* **5**, 6682 (2012).
26. H. G. Cha, J. Song, H. S. Kim, W. Shin, K. B. Yoon, and Y. S. Kang, *Chem. Commun.* **47**, 2441 (2011).
27. C. Aydin, S. A. Mansour, Z. A. Alahmed, and F. Yakuphanoglu, *J. Sol-Gel Sci. Technol.* **62**, 397 (2012).
28. Z. D. Pozun and G. Henkelman, *J. Chem. Phys.* **134**, 224706 (2011).
29. M. B. Sahana, C. Sudhakar, G. Setzler, A. Dixit, J. S. Thakur, G. Lawes, R. Naik, V. M. Naik, and P. P. Vaishnava, *Appl. Phys. Lett.* **93**, 231909 (2008).
30. P. Kumar, R. K. Singh, N. Rawat, P. B. Barman, S. C. Katyal, H. Jang, H. N. Lee, and R. Kumar, *J. Nanopart. Res.* **15**, 1532 (2013).
31. L. Lu, L. Li, X. Wang, and G. Li, *J. Phys. Chem. B* **109**, 17151 (2005).
32. K. Sivula, R. Zboril, F. L. Formal, R. Robert, A. Weidenkaff, J. Tucek, J. Frydrych, and M. Grätzel, *J. Am. Chem. Soc.* **132**, 7436 (2010).
33. N. Pailhé, A. Wattiaux, M. Gaudon, and A. Demourgues, *J. Solid State Chem.* **181**, 2697 (2008).
34. S. Chaleawlert-umpon and N. Pimpha, *Mater. Chem. Phys.* **135**, 1 (2012).
35. Z. Xin, S. Xiao-Hui, and Z. Dian-Lin, *Chin. Phys. B* **19**, 086802 (2010).
36. M. F. Al-Kuhaili, M. Saleem, and S. M. A. Durrani, *J. Alloys Compd.* **521**, 178 (2012).

37. A. D. Trolio, E. M. Bauer, G. Scavia, and C. Veroli, *J. Appl. Phys.* **105**, 113109 (2009).
38. G. P. Joshi, N. S. Saxena, R. Mangal, A. Mishra, and T. P. Sharma, *Bull. Mater. Sci.* **26**, 387 (2003).
39. P. Tyagi and A. G. Vedeshwar, *Bull. Mater. Sci.* **24**, 297 (2001).
40. L. Brus, *J. Phys. Chem.* **90**, 2555 (1986).
41. J. C. Slater, *Phys. Rev.* **103**, 1631 (1956).
42. K. L. Bray, *Top. Curr. Chem.* **213**, 1 (2001).
43. E. Güneri and A. Kariper, *J. Alloy. Compd.* **516**, 20 (2012).
44. D. K. Dwivedi, Dayashankar, B. B. Singh, and M. Dubey, *J. Non-Cryst. Solids* **356**, 1563 (2010).
45. S. Sönmezoğlu, A. Arslan, T. Serin, and N. Serin, *Phys. Scr.* **84**, 065602 (2011).
46. M. Rajendran, M. G. Krishna, and A. K. Bhattacharya, *Int. J. Mod. Phys.* **15**, 201 (2001).
47. T. Tan, Z. Liu, H. Lu, W. Liu, and H. Tian, *Opt. Mater.* **32**, 432 (2010).
48. M. Oztas, *Chin. Phys. Lett.* **25**, 4090 (2008).
49. M. Harris, H. A. Macleod, S. Ogura, E. Pelletier, and B. Vida, *Thin Solid Films* **57**, 173 (1979).
50. R. G. Shimmin, A. B. Schoch, and P. V. Braun, *Langmuir* **20**, 5613 (2004).
51. K. Kandori, N. Yamamoto, A. Yasukawa, and T. Ishikawa, *Phys. Chem. Chem. Phys.* **4**, 6116 (2002).
52. K. Brezesinski, J. Haetge, J. Wang, S. Mascotto, C. Reitz, A. Rein, S. H. Tolbert, J. Perlich, B. Dunn, and T. Brezesinski, *Small* **7**, 407 (2011).
53. B. Sun, J. Horvat, H. S. Kim, W.-S. Kim, J. Ahn, and G. Wang, *J. Phys. Chem. C* **114**, 18753 (2010).
54. B. Ahmmad, K. Leonard, Md. S. Islam, J. Kurawaki, M. Muruganandham, T. Ohkubo, and Y. Kuroda, *Adv. Powder Technol.* **24**, 160 (2013).
55. S. Benramache and B. Benhaoua, *Superlattice Microst.* **52**, 1062 (2012).
56. A. Zendehnam, M. Shirazi, S. Daulatshah, and M. Sadat, *Armenian J. Phys.* **3**, 305 (2010).
57. J. H. Lee, W. C. Song, J. S. Yi, K. J. Yang, W. D. Han, and J. Hwang, *Thin Solid Films* **431-432**, 349 (2003).
58. K. C. Preetha, K. V. Murali, A. J. Ragina, K. Deepa, A. C. Dhanya, and T. L. Remadevi, *IOP Conf. Series: Materials Science and Engineering* 43 012009 (2013).
59. L. Irimpan, V. P. N. Nampoori, P. Radhakrishnan, B. Krishnan, and A. Deepthy, *J. Appl. Phys.* **103**, 033105 (2008).
60. P. Taneja and Pushan Ayyub, *Phys. Rev. B* **65**, 245412 (2002).
61. S. T. Tan, B. J. Chen, X. W. Sun, W. J. Fan, H. S. Kwok, X. H. Zhang, and S. J. Chua, *J. Appl. Phys.* **98**, 013505 (2005).
62. K. Mörl, U. Röpke, B. Knappe, J. Lehmann, R. Perthel, and H. Schröder, *Thin Solid Films* **60**, 49 (1979).
63. A. A. Akl, *Appl. Surf. Sci.* **256**, 7496 (2010).
64. I. W. Chen and X. H. Wang, *Nature* **404**, 168 (2002).
65. Z. He and J. Ma, *J. Phys. D; Appl. Phys.* **35**, 2217 (2002).